

Surface Wettability-Directed Propulsion of Glucose-Powered Nanoflask Motors

Changyong Gao,[†] Chang Zhou,[†] Zhihua Lin,[†] Mingcheng Yang,^{*,‡} and Qiang He^{*,†}

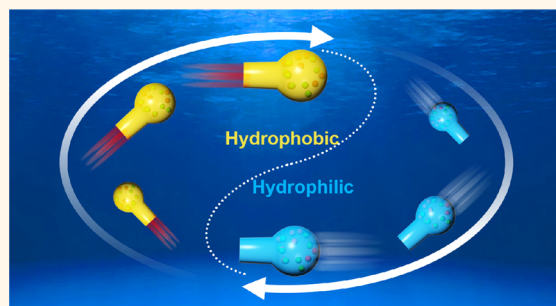
[†]Key Laboratory of Microsystems and Microstructures Manufacturing, Ministry of Education, Micro/Nanotechnology Research Centre, Harbin Institute of Technology, Yi Kuang Jie 2, Harbin 150080, China

[‡]Beijing National Laboratory for Condensed Matter Physics and Key Laboratory of Soft Matter Physics, Institute of Physics, Chinese Academy of Sciences, Beijing 100190, China

Supporting Information

ABSTRACT: Chemically driven colloidal motors capable of implementing different movements under a common environment are of great importance for various complex tasks. However, the key parameters underlying different motion behaviors are incompletely understood. Here, we demonstrate that carbonaceous nanoflask (CNF) motors move spontaneously in glucose powered by the cascade reaction of glucose oxidase and catalase, and their directional propulsion can be premeditated by controlling the surface wettability of nanomotors. The hydrophilic CNF motors move from the round-bottom to the opening neck (backward), whereas the hydrophobic CNF motors swim from the opening neck to the round-bottom (forward). We demonstrate that the backward motion of the hydrophilic CNF motors is driven by the local glucose gradient due to self-diffusiophoresis, and the forward movement of the hydrophobic CNF motors is caused by the locally produced glucose acid gradient. The fluid simulation reveals that the hydrophilic and hydrophobic CNF motors correspond to the puller and pusher models, respectively. Our study offers a minimal strategy to manipulate the direction of motion of motors for specific applications and to change the hydrodynamic behaviors of glucose-powered motors.

KEYWORDS: colloidal motor, self-propulsion, phoresis, enzymatic catalysis, flow simulation



Motility is one of the most important achievements of biological evolution and is essential for living activities.¹ For instance, bacteria such as *E. coli* can propel themselves and adjust the direction of motion through the conversion of chemical energy into mechanical force for foraging, reproducing, and forming colonies.² Inspired by motile bacteria systems, chemically powered micro- and nanomotors capable of transducing chemical energy to a mechanical motion have been developed^{3–10} and also exhibit promising applicability in diverse fields including active cargo transport,^{11,12} environmental remediation,^{13,14} sensing,^{15,16} and nanorobotics.¹⁷ In particular, the potential application of these micro- and nanomotors in biomedical fields such as actively targeted drug delivery,^{18,19} disease diagnosis,²⁰ and minimally invasive surgery²¹ is of great interest but is often limited by either the commonly used toxic fuels (e.g., hydrogen peroxide) or their unavailability in living organisms in practice.^{22,23} Recently, the use of catalase, urease, and glucose oxidase has been shown to propel colloidal particles *in vitro*,^{24–28} and thus enzymatically catalysis-induced force generation becomes an attractive solution to perform specific tasks in living organisms owing to the advantages of fuel bioavailability, versatility, and biocompatibility.^{29–31} However,

the development of enzyme-driven micro- and nanomotors remains in an early stage; the fundamental knowledge on their real propulsion mechanism is still under debate as summarized in a recent review paper.³² In addition, it is challenging to modulate the self-propelling direction of enzyme-driven nanomotors under the same chemical reactions and environment, which is relevant for performing various complex tasks.

Herein, we report a glucose-powered carbonaceous nanoflask (CNF) motor autonomously moving in a solution of glucose as directed by its surface wettability. The CNFs were first synthesized by using a soft template-based polymerization method and then glucose oxidase (GOx) and catalase (Cat) were loaded into the cavity of the hydrophilic or hydrophobic CNFs. The flask architecture permits the encapsulation of catalysts and the free diffusion of reactants and products only through the narrower tubular neck with an opening at the tip, which guarantees the generation of local gradient in the chemical potential across the motors. In the presence of

Received: June 16, 2019

Accepted: October 17, 2019

Published: October 17, 2019

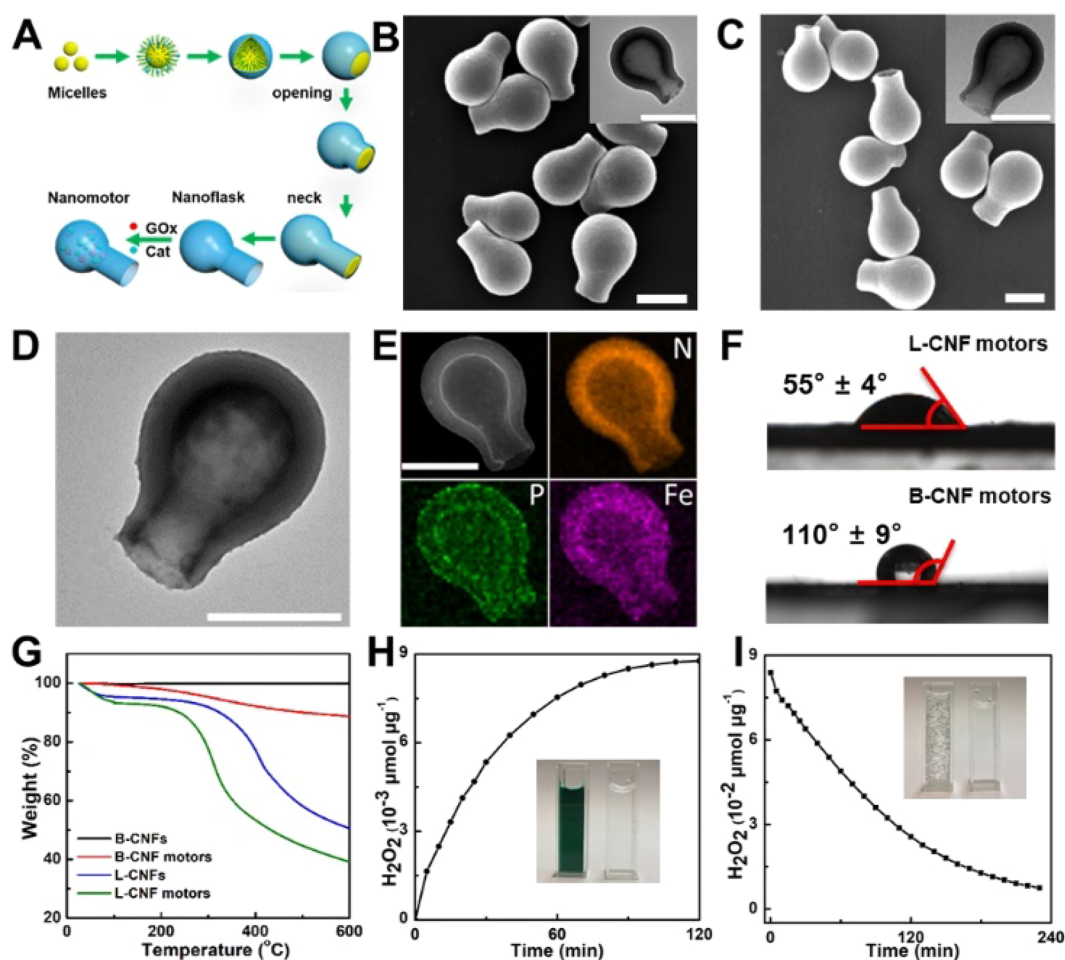


Figure 1. Fabrication and characterization of the enzyme-loaded round-bottom CNF motors. (A) Schematic illustration of the fabrication process of hydrophilic CNF (L-CNF) motors. (B) SEM image of as-synthesized L-CNFs. The inset is the TEM image of a single L-CNF. (C) SEM image of as-obtained hydrophobic CNF (B-CNF) motors. The inset is the TEM image of a B-CNF. (D) Negative staining TEM image of an enzyme-loaded L-CNF motor. (E) STEM and corresponding EDX mapping images of the enzyme-loaded L-CNF motor. (F) The water contact angle measurement of an L-CNF monolayer and a B-CNF monolayer. (G) Thermogravimetric analysis of the L- and B-CNF particles and motors. (H) GOx activity assay of L-CNF motors. (I) Cat activity assay of L-CNF motors. Scale bars: 500 nm.

glucose, the hydrophobic CNF motors autonomously swim from the opening neck toward the round-bottom (forward), while the hydrophilic CNF motors move from the round-bottom toward the opening end (backward). We find that the self-propulsion is mainly caused by the GOx-catalytic reaction (β -D-glucose \rightarrow D-glucose acid + H_2O_2), and the backward movement of CNF motors is dominated by the local glucose gradient whereas the forward motion of the CNF motors is mainly propelled by the generated local glucose acid gradient. Moreover, the hydrophilic and hydrophobic CNF motors correspond to the classic puller and pusher models as demonstrated by the flow field simulation. These findings provide insights into the understanding of the role of the surface wettability of motors on the directional motion of chemically powered colloidal motors and offer a simple method to control the directional motion of micro-/nano-motors for potential applications.

RESULTS AND DISCUSSION

The preparation process of the CNF motors with surface hydrophilicity is schematically illustrated in Figure 1A. First, the hydrophilic CNFs (denoted as L-CNFs) were synthesized by using a soft template-based polymerization method.³³ The

hydrophobic CNFs (denoted as B-CNFs) were obtained by the carbonization of L-CNFs at 900 °C for 1 h. Then, GOx and Cat were encapsulated in the cavity of CNFs through the opening by using a vacuum infusion method. The scanning electron microscopy (SEM) image in Figure 1B shows that the L-CNFs have well-defined flask structure with a length of 844 ± 44 nm. The inset transmission electron microscopy (TEM) image exhibits a hollow structure with a single open neck. The inner diameters of the hollow cavity and nanoneck were 559 ± 31 nm and 185 ± 51 nm, respectively. The statistical analysis of the size distribution shows that the error of the average length of the nanoflasks prepared in different batches was 17 nm, indicating the good reproducibility of the nanoflasks. The SEM and the inset TEM images of B-CNFs show that the thermal treatment did not obviously change their structure and size (Figure 1C). By depositing CNFs on a glass surface, we found that the contact angle changed from $52 \pm 4^\circ$ to $109 \pm 5^\circ$ after thermal treatment (Figure S1). Although it may not be accurate, it still demonstrates that the L-CNFs were hydrophilic and the B-CNFs were hydrophobic, indicating the different surface wettabilities of CNFs. To prepare glucose-powered CNF motors, the L-CNFs and B-CNFs were dispersed into a phosphate buffer solution containing GOx

and Cat under a vacuum condition, respectively. The negative staining TEM image shows the appearance of cloudy regions, suggesting the successful encapsulation of enzymes in the cavity of L-CNF motors (Figure 1D). The scanning transmission electron microscopy/dispersive X-ray (STEM-EDX) spectroscopic mapping images further reveal the presence of phosphorus (P) and iron (Fe) elements in the L-CNF motor, which comes from the GOx and the Cat, respectively (Figure 1E). Note that, in order to avoid the influence of phosphate on elemental analysis, water was used as dispersing enzyme during EDX analysis. Figure S2 demonstrates that the GOx and Cat were also encapsulated into B-CNF motors. To confirm the absence of enzymes on the surface of the nanoflask motors, the outer surface of nanoflasks before and after the enzyme encapsulation was examined by using SEM. The SEM images show that the surface morphologies of nanoflasks and nanoflask motors were similar, indicating that none of the enzymes existed on the outer surface of the motors (Figure S3). In addition, the as-prepared L-CNF and B-CNF motors retained their original surface wettability (Figure 1F).

We next evaluated the loading amount of GOx and Cat, and their enzymatic activity in motors. The thermogravimetric analysis (TGA) results in Figure 1G show that the weight loss of L-CNF motors, L-CNFs, B-CNF motors, and B-CNFs was 60.82%, 49.44%, 11.46%, and 0.15%, respectively. Since the weight losses in TGA test are associated with either water or the organic molecules,³⁴ the amount (in weight) of enzyme loading is thus estimated to be 11.38% in L-CNF motors and 11.31% in B-CNF motors, respectively. To evaluate the enzyme encapsulation efficiency, the concentration of two enzymes before and after loading was calculated. It was shown that the enzyme encapsulation efficiency was about 6.37%. We also found that the enzyme content in the CNF motors increased with the increase of perfusion times, indicating that the enzyme loading efficiency could be regulated by controlling the perfusion times (Figure S4). The enzymatic activity inside the motors was examined by UV-vis spectroscopy.³⁵ It can be found that the bioactivities of GOx-coupled L-CNF motors and B-CNF motors were 1.75×10^{-4} and 1.71×10^{-4} μmol glucose per μg motors-min (Figure 1H and Figure S5). The bioactivities of Cat-coupled L-CNF motors and B-CNF motors were 5.82×10^{-4} and 6.06×10^{-4} μmol H_2O_2 per μg motors-min (Figure 1I and Figure S6). These results indicate that the entrapped GOx and Cat remained active, and both the substrate and the product were able to diffuse in and out through the opening. Taken together, these results suggest that two types of CNF motors with different surface wettabilities were successfully fabricated.

The motility of CNF motors was characterized by using optical microscopy. First, we investigated the motion behavior of L-CNF motors in 10 mM glucose solution. The time-lapse images show that the L-CNF motor moved along a direction from the round-bottom to the opening neck (backward) at a speed of $0.97 \mu\text{m s}^{-1}$ (Figure 2A and Video S1). Figure 2B shows the typical trajectories of L-CNF motors in different concentrated glucose solutions. In the absence of glucose, the L-CNF motors displayed a typical Brownian motion without a directional movement. With the increase of glucose concentration, the displacement of L-CNF motors gradually increased, indicating an enhanced active diffusion. Then, we studied this enhanced motion by calculating the mean square displacement (MSD). In all cases, at least 15 motors were analyzed per condition. The value of MSD as a function of

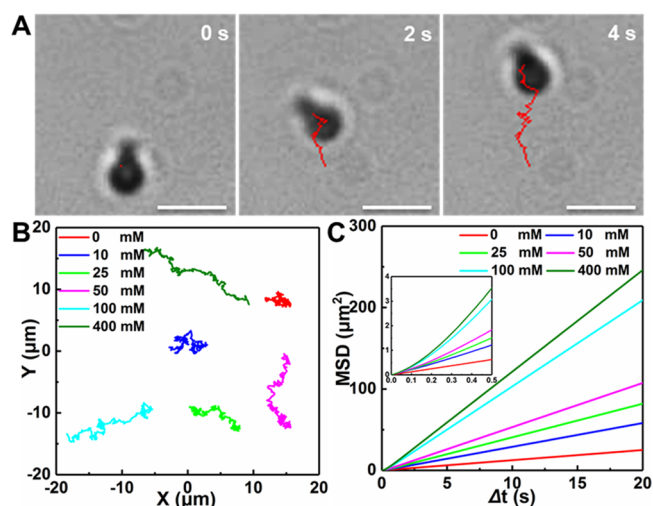


Figure 2. Dynamics of L-CNF motors. (A) Time-lapse images of L-CNF motors swimming in 10 mM glucose solution. Scale bars: 1 μm . (B) Extracted trajectories of L-CNF motors in different glucose concentrations in 20 s. (C) Curves of the MSD versus Δt at different glucose concentrations. Inset: enlarged curves of MSD versus short time scale.

time interval (Δt) is plotted in Figure 2C. It is evident that the MSD versus Δt curve was linear in the absence of glucose, which is a feature of Brownian motion.^{36,37} In contrast, the MSD curves displayed a parabolic shape, in which the slopes went up with increasing glucose concentrations. For a self-propelled colloidal motor, the MSD versus Δt curve follows a quadratic relationship in a short-time scale and then a linear relationship in a long-time scale.³⁸ Since there are only the enzymatic cascade reactions in this system, we speculate that the self-propelling movement of L-CNF motors is powered by the enzymatic reaction.

The directional motion was also investigated by tracking the longitudinal coordinates of L-CNF motors; the travel angular change ($\Delta\theta$) and the angle between the directions of subsequent movements ($\Delta\phi$) were defined as schematically illustrated in Figure 3A. The magnitude of $\Delta\theta$ represents the directional movement capacity of colloidal motors. By plotting the mean squared angular displacement (MSAD) as a function of time interval, Δt , in which the MSAD was calculated as $\text{MSAD} = \langle \Delta\theta(t)^2 \rangle = 2D_r\Delta t$ (D_r , rotational diffusion coefficient), one can see that with the increasing glucose concentration, the slopes gradually decreased, suggesting a directional movement of L-CNF motors (Figure 3B). Furthermore, the turning angle distribution (TAD) during the movement was calculated by measuring the $\Delta\phi$. Figure 3C shows that the TAD displayed an equal distribution of direction across all angles in the absence of the glucose. In the presence of glucose, notable peaks were observed at 0° , and the TAD at 0° gradually increased with the increasing glucose concentrations. These results demonstrate the directional motion of L-CNF motors was powered by the enzymatic reaction and the self-propelling force was dependent on the intensity of chemical reaction. It is noted that the higher glucose concentration used is in order to improve the viscosity so that we could better observe the change of the directional motion of nanoflask motors.

To explore the contribution of enzymatic reactions on the driving force of CNF motors, the motion behaviors of GOx or

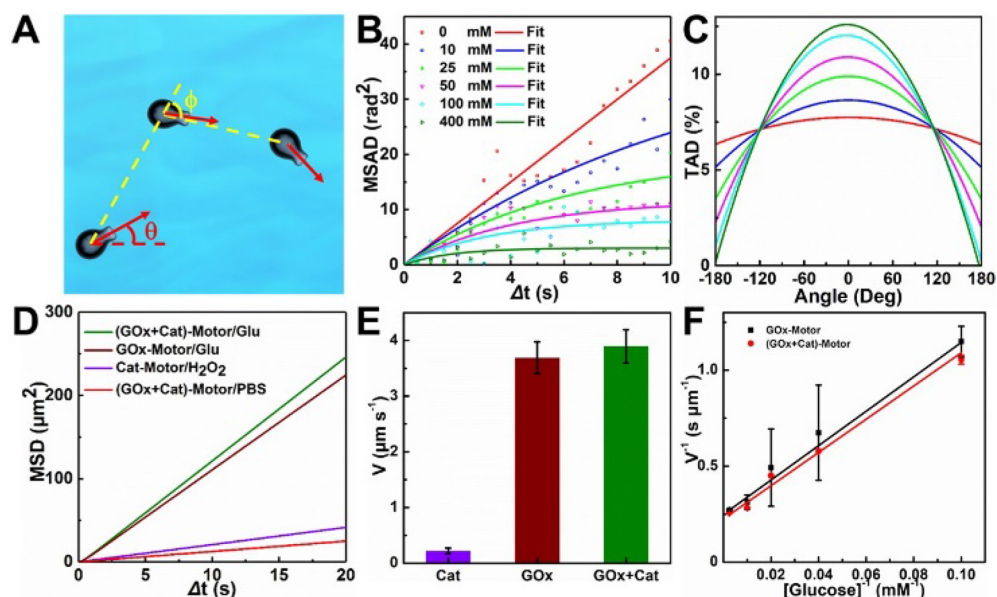


Figure 3. Movement analysis of L-CNF motors. (A) Scheme of the self-propulsion of L-CNF motors for two subsequent time steps. (B) Mean squared angular displacement (MSAD) as a function of time interval (Δt). (C) Turning angle distribution (TAD) of L-CNF motors under different glucose concentrations in a time interval of 3 s. (D) MSD analysis and (E) the corresponding propulsion velocity of three types of L-CNF motors in different substrates. (F) Lineweaver–Burk plots of the movement of two types of L-CNF motors under different glucose concentrations.

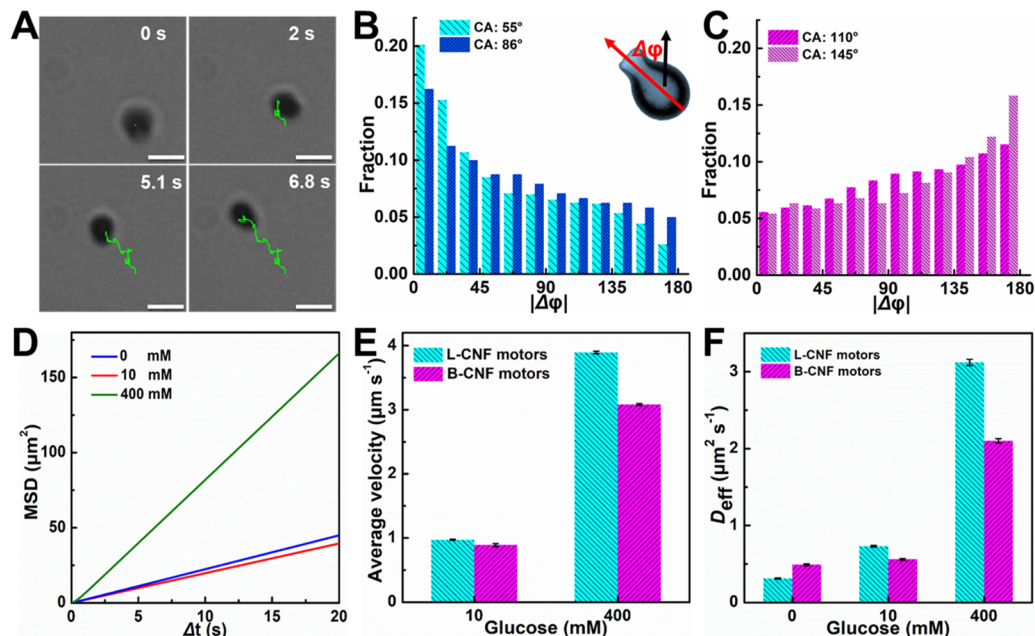


Figure 4. Comparison of the motion parameters of L-CNF motors and B-CNF motors. (A) Time-lapse images of the movement of single B-CNF motors in 10 mM glucose solution. Scale bars: 1 μm . The angle distribution between the polarity of (B) L-CNF and (C) B-CNF motors and their motion direction with different contact angles. Inset: movement direction (black arrow), polarity (red arrow). (D) MSD analysis of B-CNF motors at different glucose concentrations. (E) Comparison of the velocities between L-CNF and B-CNF motors. (F) Effective diffusion coefficient (D_{eff}) values of L-CNF and B-CNF motors measured from the slopes of the linear fitting plots of their respective MSD curves.

Cat loaded L-CNF motors were investigated. For Cat-loaded L-CNF motors, the H_2O_2 solution was limited to 1 mM that is comparable with the generated H_2O_2 concentration in the cascade reaction of GOx and Cat. The MSD curves of three types of L-CNF motors as a function of Δt show that the slope of the MSD curve of GOx-loaded L-CNF motors (i.e., GOx-motor) was almost similar to that of GOx and Cat-loaded L-

CNF motors (i.e., (GOx+Cat)-motors) in the 400 mM glucose solution. However, the slope of the MSD curve of Cat-loaded L-CNF motors (i.e., Cat-motor) in H_2O_2 solution was very small, close to that of (GOx+Cat)-motors in PBS (phosphate buffer saline) (Figure 3D). It seems that the self-propelling motion of L-CNF motors is mainly contributed by the GOx-catalyzed reaction. Similarly, Figure 3E displays that the self-

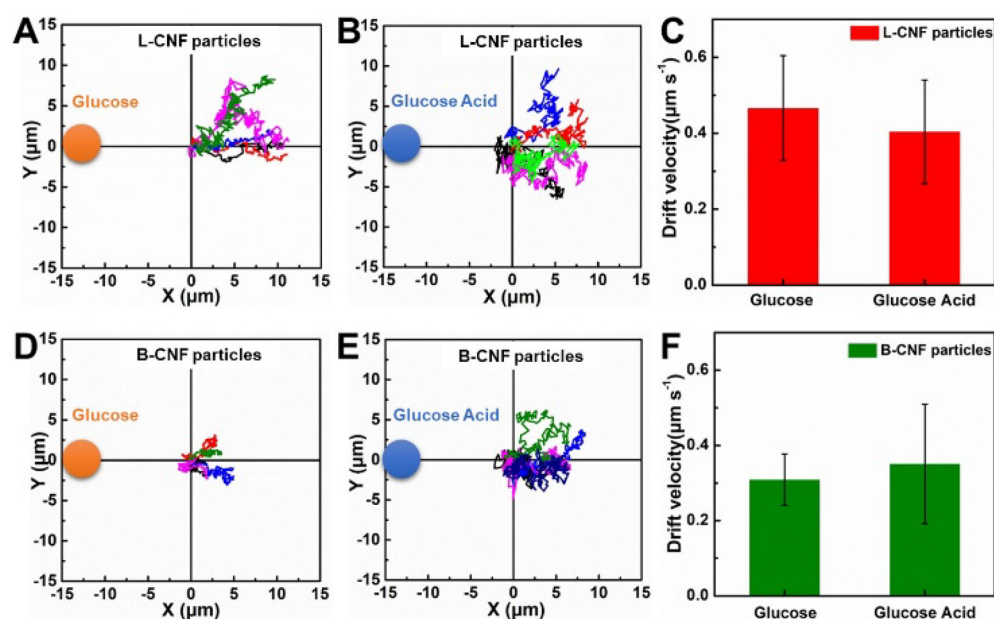


Figure 5. Motion of the passive L-CNF and B-CNF particles in external chemical gradients. Trajectories of passive L-CNF particles in (A) external glucose and (B) glucose acid gradients, with the tracking period 20 s. (C) Comparison of diffusiophoretic velocities of the passive L-CNF particles in glucose and glucose acid gradients. Trajectories of passive B-CNF particles in (D) external glucose and (E) glucose acid gradients. (F) Comparison of diffusiophoretic velocities of the passive B-CNF particles in glucose and glucose acid gradients.

propelling velocities of the above-mentioned (GOx+Cat)-motors, GOx-motors, and Cat-motors are 3.89 ± 0.29 , 3.69 ± 0.28 , and $0.22 \pm 0.05 \mu\text{m s}^{-1}$, respectively, indicating the contribution of Cat-catalyzed reaction may be neglected. The similar motion behaviors were also found in the single enzyme (GOx or Cat) and two enzymes encapsulated B-CNF motors, where the velocity of (GOx+Cat)-encapsulated motors is similar to that of GOx-loaded motors and obviously higher than that of Cat-encapsulated motors (Figure S7). Furthermore, the maximum propulsion velocity (V_{max}) and the Michaelis–Menten constant (K_{m}) were calculated by using a Lineweaver–Burk plot.³⁹ It can be seen that the V_{max} and K_{m} values of GOx-motors and (GOx+Cat)-motors had no significant difference (Figure 3F). Taken together, these data demonstrate that the self-propulsion of L-CNF motors is mainly contributed by the GOx-catalytic decomposition of glucose.

Next, we investigated the motion behaviors of B-CNF motors. The time-lapse images show that the B-CNF motors moved from the opening to the bottom (forward) in 10 mM glucose solution at a speed of $0.82 \mu\text{m s}^{-1}$, indicating an opposite movement direction with L-CNF motors (Figure 4A and Video S2). To confirm our observation, new nanoflask motors with a water contact angle of $86 \pm 3^\circ$ and $145 \pm 5^\circ$ were prepared by the carbonization of L-CNFs at 600°C for 1 h and 900°C for 2 h, respectively. Then, the angle $\Delta\phi$ between the polarity of motors and the direction of motion in 400 mM glucose solution over a period of 50 s was measured (Figure 4B and 4C). It is evident that the L-CNF motors tended to move backward, while the B-CNF motors tended to move forward. Furthermore, with the increase of the contact angle of the CNF motors, the direction of motion of motors gradually changed from backward to forward, indicating that there may be a transition contact angle between 86° and 110° at which the CNF motors have no specific directional motion. In addition, we found that the neck of the CNF motors also had an effect on the movement of the CNF motors. Moreover,

the MSD versus Δt curves in Figure 4D show that the active diffusion of B-CNF motors enhanced with the increasing glucose concentrations. However, the velocities of B-CNF motors were lower than that of L-CNF motors under the same glucose concentrations (Figure 4E). This is mainly because the strength of the interaction between the motor and solute (glucose or glucose acid) of the B-CNF motors is lower than that of the L-CNF motors.⁴⁰ We further calculated the effective diffusion coefficient (D_{eff}) of motors according to the equation $\text{MSD} = 4D_{\text{eff}}\Delta t$. Figure 4F shows that the D_{eff} values of B-CNF motors were smaller than that of L-CNF motors. Note that the Brownian diffusion of B-CNF motors is stronger than L-CNF motors in the absence of glucose, which is reasonable since the hydrophobic surface may reduce the viscous drag.⁴¹ Furthermore, the motion behaviors of both the L-CNF motors and B-CNF motors appeared as “run and tumble” model similar to that of bacteria. The possible reason is that the flask-like structure of motors has an effect on the diffusion of glucose and gluconic acid, which leads to the periodic movement of both the L-CNF motors and B-CNF motors. Taken together, these results show that these two types of CNF motors have different motion directions and velocities under the same conditions.

As mentioned above, the propulsive force is mainly contributed by the GOx-catalytic reaction. Thus, it can be reasonably speculated that the underlying driving mechanism of the motors is the self-diffusiophoretic effect generated by the local concentration gradients of the reactant (i.e., glucose) and the product (i.e., glucose acid) across the motors. In view of this, we explored the effect of glucose and glucose acid concentration gradients on the motion behavior by performing independent control experiments, where passive CNF particles without addition of both GOx and Cat were suspended in an externally applied glucose (or glucose acid) gradient, ∂c , as displayed in Figure 5. We found that both the hydrophilic L-CNF and hydrophobic B-CNF particles moved against the chemical gradients (Figure 5A, 5B, 5D, 5E) due to

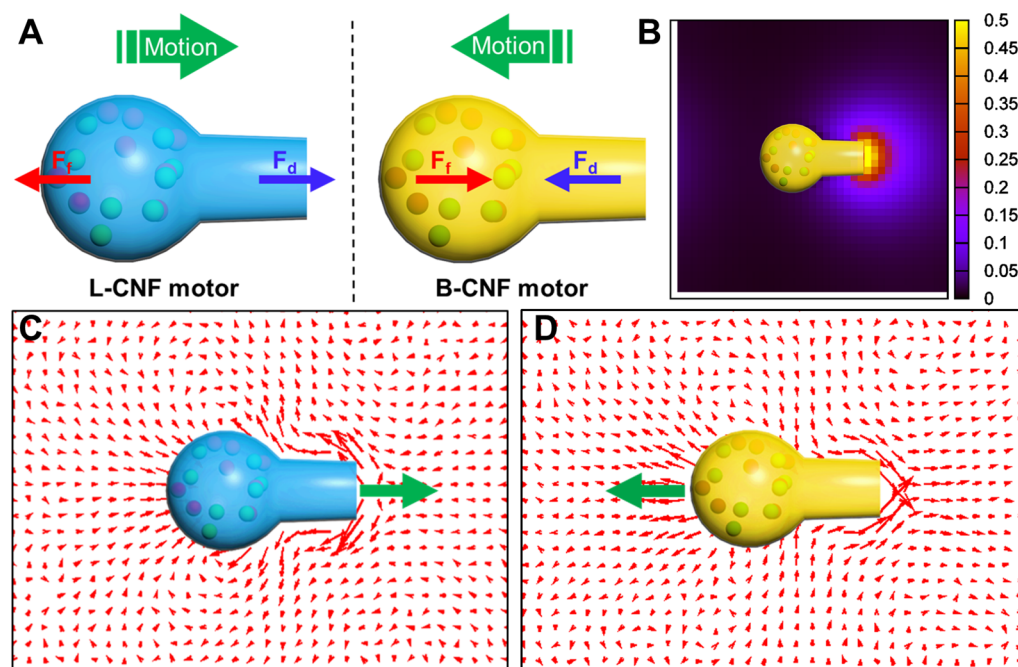


Figure 6. Flow field simulation of L-CNF motors and B-CNF motors. (A) Sketched driving forces F_d and frictions F_f on the L-CNF motor (left) and B-CNF motor (right) exerted by the fluids due to the self-generated chemical gradients. (B) Concentration distribution of the reaction products induced by the biocatalytic reactions. (C) Puller-like flow fields around the self-diffusiophoretic L-CNF motor, where the small red arrows refer to the flow velocity and the large green arrow to the direction of motion. (D) Pusher-like flow fields around the self-diffusiophoretic B-CNF motor. The concentration and flow fields are obtained by mesoscale simulations.

diffusiophoresis, $v = -\mu\alpha\partial c$ with v the drift velocity, μ the particle mobility, and α defined as the diffusiophoretic factor. Interestingly, the L-CNFs drift faster in the glucose gradient ($0.47 \mu\text{m s}^{-1}$) than in the glucose acid gradient of the same magnitude ($0.4 \mu\text{m s}^{-1}$) (Figure 5C), while the B-CNFs drift faster in the glucose acid gradient (Figure 5F). This means that the diffusiophoretic factor of the hydrophilic L-CNFs in the glucose gradient is larger than that in the glucose acid gradient, $\alpha_{\text{glu}} > \alpha_{\text{acid}}$. In contrast, for the hydrophobic B-CNFs the situation is reversed, namely $\alpha_{\text{glu}} < \alpha_{\text{acid}}$.

Based on these observations, it is straightforward to analyze the active motion of the L- and B-CNF motors in terms of the self-diffusiophoresis. Since the diffusivity of the glucose is similar to that of glucose acid, their local concentration gradients self-generating around the CNF motor have the same magnitude but in opposite direction. Thus, the self-propelled velocity of the CNF motor approximately reads $v = \mu(\alpha_{\text{glu}} - \alpha_{\text{acid}})\partial c$, with ∂c being the self-generated local concentration gradient of the glucose acid. Therefore, the hydrophilic L-CNF motors self-propel along the local gradient in the glucose acid, i.e. moving with the flask opening forward, whereas the hydrophobic B-CNF motors self-propel with the flask bottom forward. This prediction of the directional propulsion is well consistent with the experimental results in Figures 4B and 4C. Note that the self-generated local gradients across the CNF motors are an order of magnitude larger than the externally applied ones, so the CNF motors can easily achieve the self-propelling speed as measured in the above experiments (Figure 3E and Figure 4E). To investigate the effect of the size of the neck of the nanoflask motors on the mechanism of the motion, two kinds of L-CNF motors with a neck length of 31 ± 14 nm and 486 ± 33 nm were fabricated by controlling the hydrothermal reaction time for 8 and 21 h, respectively (Figure S8). We found that both of the L-CNF motors

displayed backward motion, indicating the length of the neck of the CNF motor has no obvious effect on the motion mechanism.

The hydrophilic L-CNF motors and hydrophobic B-CNF motors exhibit the opposite direction of self-propelled motion, which should essentially generate different flow fields around them. To examine this, we analyzed the forces on the L- and B-CNF motors, as sketched in Figure 6A. Since the chemical reactions occur inside the CNF motors, the chemical gradients should be the maximum near the flask opening, and thus the self-diffusiophoretic force (driving force), $F_d = -\alpha\partial c$, is mainly applied on the motor surface around the flask opening. On the other hand, the flask bottom is significantly larger than the opening such that the friction, $F_f = -v/\mu$, from the fluid, is mainly exerted on the bottom part of the CNF motors. In the stationary state, the driving force is balanced by the friction. As such, in terms of the experimental results and the related discussions above, the hydrophilic L-CNF motor is subject to a positive force dipole, while the hydrophobic B-CNF motor suffers from a negative force dipole (Figure 6A). Due to Newton's third law, the L-CNF motor thus exerts a negative force dipole on the surrounding fluid and hence generates a puller-like flow field. Reversely, the B-CNF motor exerts a positive force dipole on the surrounding fluid so as to induce a pusher-like flow field.

In order to verify the speculation on the flow fields, we performed mesoscale dynamics simulation of the CNF motors, where the model CNF motors have the similar geometry and propulsion mechanism to the experimental ones. For convenience, the catalytic reaction is imposed at the flask opening instead of its inside. Under the self-generated chemical gradients around the opening of the nanoflasks (Figure 6B), the CNF motors swim along the symmetric axis due to the self-diffusiophoresis. The simulation results indeed show that the

flow fields around the L-CNF motor (Figure 6C) and B-CNF (Figure 6D) are puller- and pusher-like, respectively. It is noted that although the change of surface wettability of the CNF nanoflask motors accompanies the change of their surface potential (L-CNF: ~ 30 mV; B-CNF: ~ 10 mV), the experimental results and simulation demonstrate that the directional change of the CNF motors is ascribed to the change of local flow field on the surface of the CNF motors. In other words, the self-diffusiophoresis is independent of the surface potential of the CNF motors; we thus believe that the changes in the direction of motion are determined by the difference of the surface wettability of the CNF nanoflask motors. Therefore, only by changing the surface wettability of the CNF motors did we achieve a transition from the puller to pusher, without affecting any other properties of the CNF motors and the solvent. This would provide us an opportunity to exclusively investigate the hydrodynamic behaviors of the pushers and pullers, which are fundamentally different.

CONCLUSION

In this work, we have demonstrated that carbonaceous nanoflask motors swim autonomously in the solution of glucose as directed by their surface wettability alone. The enzymatic cascade reaction of glucose oxidase and catalase occurring inside the nanoflask propelled the motors, where the hydrophilic nanoflask motors moved with relatively high speed from the round-bottom to the opening neck (backward), while the hydrophobic nanoflask motors swim with lower speed from the opening neck to the round-bottom (forward). Further investigation reveals that the backward motion was mainly propelled by the local glucose concentration gradient, and the forward movement was dominated by the produced glucose acid gradient. The simulation results reveal that the hydrophilic nanoflask motor generates a puller-like flow field, whereas the hydrophobic motor creates a pusher-like flow field. It suggests that a transition from the puller to pusher could be achieved only by changing the surface wettability of motors. These results provide a deeper knowledge on the fundamental aspects underlying enzyme-driven motors and offer a minimal strategy to manipulate the direction of movement of micro-/nanomotors in future applications.

EXPERIMENTAL SECTION

Materials. Sodium oleate (SO), poly(ethylene glycol)-*block*-poly(propylene glycol)-*block*-poly(ethylene glycol) (EO₂₀-PO₇₀-EO₂₀, P123), ribose, glucose oxidase (GOx), phosphate buffer saline (PBS), (NH₄)₂C₂O₄·H₂O, KHCO₃, uranyl acetate, bovine liver catalase (Cat), glucose, and hydrogen peroxide were purchased from Sigma-Aldrich. All chemicals were used without further purification. Ultrapure water (Millipore) of 18.2 M Ω -cm was used for all experiments.

Preparation of Hydrophilic Nanoflask Motors. To prepare glucose-powered hydrophilic carbonaceous nanoflask (L-CNF) motors, L-CNF particles with hydrophilic surface were first synthesized according to the published method.⁴² Briefly, 0.0365 g of SO and 0.0435 g of P123 were mixed in 20 mL of deionized water and stirred at 200 rpm for 30 min. Under the same stirring conditions, 3 g of ribose was dissolved in 40 mL of deionized water, followed by mixing with the above solution. After stirring at 500 rpm for 30 min, the obtained transparent solution was transferred into a 100 mL volume autoclave and then hydrothermally treated at 160 °C. After 12 h, the autoclave was cooled to room temperature and the resulting products were collected by centrifugation at 9500 rpm for 15 min. The precipitates were washed with deionized water for five times and then the obtained L-CNF particles were dried and stored. To fabricate

CNF particles with short and long neck lengths, the hydrothermal reaction time was controlled for 8 and 21 h, respectively.

The L-CNF motors were prepared via a vacuum infusion method. First, the hollow L-CNF particles (10 mg) were added in 5 mL of the PBS solution containing GOx and Cat (3 mg mL⁻¹ and 1 mg mL⁻¹, respectively). Then, the obtained suspension was transferred into a steel chamber. After sealing the chamber from the surrounding air, the chamber was placed under vacuum to a pressure of 10⁵ Pa for 6 h by using a mechanical pump. To remove the excess enzymes from the solution and the outside surface of particles, L-CNF motors were washed with PBS five times. During each cleaning process, the supernatants were discarded and the resulting precipitations were collected by centrifugation at 9500 rpm for 15 min. Afterward, the GOx and Cat loaded L-CNF motors were collected and then stored at 4 °C for further experiments.

Preparation of Hydrophobic Nanoflask Motors. In order to fabricate glucose-powered hydrophobic carbonaceous nanoflask (B-CNF) motors, B-CNF particles were first prepared. Typically, a mixture containing 1 g of L-CNF particles, 4 g of (NH₄)₂C₂O₄·H₂O, and 4 g of KHCO₃ was thoroughly mixed for 45 min. Under the protection of N₂, the sample was calcined to 600 °C at a rate of 10 °C min⁻¹ and kept for 1 h. At a heating rate of 5 °C min⁻¹, the mixture was further calcined to 900 °C. One hour later, the carbonization was stopped and the treated sample was cooled and then dissolved in 1 M HCl solution overnight. The B-CNF particles were collected by centrifugation and washed with deionized water. Based on the same enzyme loading method, B-CNF motors were prepared by loading GOx and Cat into the B-CNF particles.

Preparation of Concentration Gradients. To prepare the concentration gradients of glucose and gluconic acid, small pieces of cylindrical agarose gel (1 mm³) were first cut and soaked overnight in the glucose (400 mM) and gluconic acid (400 mM) solution, respectively. Then, the glucose or gluconic acid-loaded agarose gel was placed on the edge of a Petri dish filled with PBS solution to establish glucose and gluconic acid gradients.

Autonomous Movement of CNF Motors. To propel the nanoflask motors, L-CNF motors and B-CNF motors were dropped into glucose solutions with a pH value of 6.5 and a temperature of 25 °C. The motion of glucose-powered CNF motors was observed by using an Olympus IX71 inverted microscope. The nanomotor suspensions containing different glucose concentrations were dropped in a Petri dish, respectively. To minimize the drifting effect, the Petri dishes were sealed during observation. The movement movies were recorded with a CCD camera.

Movement Analysis. Accurate tracking of the glucose-powered CNF motors was accomplished by using the software of Image J and analyzed using Origin 8.0. Then, the mean-square-displacement (MSD) was calculated with $\text{MSD}(\Delta t) = \langle (x_i(t + \Delta t) - x_i(t))^2 \rangle$ ($i = 2$), where x is a two-dimensional vector and i is an index to show x and y . The effective diffusion coefficient (D_{eff}) was extracted with $D_{\text{eff}} = \text{MSD} / (4\Delta t)$. In all cases, at least 15 CNF motors were analyzed.

Characterization. The encapsulated enzymes were characterized by using transmission electron microscopy (TEM) and scanning transmission electron microscopy/dispersive X-ray (STEM-EDX) spectroscopic mapping. The CNF motor suspension was dropped onto a copper grid and then negatively stained with 1% uranyl acetate. After excess solution was wicked away, the motors were imaged using Tecnai G2 Sphera (FEI) microscopy. Scanning electron microscopy (SEM) was carried out using a Quanta 200 FEG microscope. Thermogravimetric analysis (TGA) of nanomotors was done by heating particles from 25 to 600 °C at a heating rate of 10 °C min⁻¹ under a N₂ atmosphere.

Mesoscale Simulation. To simulate the self-diffusiophoretic nanoflask motor, a hybrid mesoscale simulation scheme was used to bridge the huge time- and length-scale gaps between the fluid and colloidal particles. Here, the fluid is simulated by multiparticle collision dynamics (MPC),^{43,44} while the CNF motor is described by standard molecular dynamics (MD).

In the MPC part, the fluid is coarse grained into N point particles of mass m . The particle dynamics consists of alternating streaming

and collision steps. In the streaming step, the fluid particles move ballistically for a time h . In the collision step, the particles are sorted into a cubic lattice with cells of size a and interact with each other via the Anderson-thermostat collision rule.^{45,46} The collision-cell grid is randomly shifted before each collision step to ensure Galilean invariance. This method can properly capture hydrodynamic interactions, thermal fluctuations, dissipation, and the mass diffusion process. In the simulations, the units are reduced by setting $m = 1$, $a = 1$, and the system temperature $k_B T = 1$ with k_B the Boltzmann constant. We employ MPC parameters $h = 0.1$ and the mean number of fluid particles per cell $\rho = 15$. The simulation system is a cube of size 40, with periodic boundary conditions applied in all the directions.

In the MD part, the CNF motor is a rigid body, constructed by a large sphere of radius $R_l = 4$ and two small spheres of radius $R_s = 2.4$. The mass density of the sphere is the same as that of the fluid. In order to model the self-diffusiophoresis of the CNF motors, we consider a fluid mixture consisting of three components A, B and C, where A and B represent the solute molecules, and C represents the solvent. The chemical reactions occur at the flask opening with a certain probability.⁴⁷ The reactants are simultaneously fed into the solution by performing inverse reaction in regions far away from the CNF motors. Thus, the chemical reactions generate a local chemical gradient around the CNF motors. The fluid particles of different species interact with the beads of the nanoflask via different potential interactions, which leads to the self-diffusiophoresis of the nanoflask. Specifically, the fluid particles couple with the spheres through a repulsive Lennard-Jones (LJ) type of potential,

$$U(r) = 4\epsilon \left[\left(\frac{\sigma}{r} \right)^6 - \left(\frac{\sigma}{r} \right)^3 \right] + \epsilon, \quad r \leq r_c$$

where r is the distance between the beads and the fluid molecule, the interaction length $\sigma = 4$ for the large sphere and $\sigma = 2.4$ for the small bead, the cutoff $r_c = 2^{1/3}\sigma$, and the potential intensity $\epsilon_A = \epsilon_C = 2$ and $\epsilon_B = 0.5$. When the catalytic reaction occurring on the bead surface is $A \rightarrow B$, the CNF motors experience a self-diffusiophoretic motion toward the opening, since the reaction product (species B) has a high concentration around the flask opening and a weak repulsion with the nanoflask. Otherwise, for the catalytic reaction of $B \rightarrow A$, the self-diffusiophoretic motion reverses. The dynamics of the CNF motor and its neighboring fluid particles evolves according to the Newton equations of motion integrated by the velocity-Verlet algorithm with a time step $\Delta t = 0.002$.

ASSOCIATED CONTENT

Supporting Information

The Supporting Information is available free of charge on the ACS Publications website at DOI: [10.1021/acsnano.9b04708](https://doi.org/10.1021/acsnano.9b04708).

Additional information, including water contact angle, characterization of hydrophobic nanoflask nanomotors, SEM and TEM images, GOx and Cat activity assays, and propulsion velocity (PDF)

Self-propelled motion of L-CNF motors (AVI)

Motion of B-CNF motors (AVI)

AUTHOR INFORMATION

Corresponding Authors

*E-mail: mcyang@iphy.ac.cn.

*E-mail: qianghe@hit.edu.cn.

ORCID

Changyong Gao: [0000-0001-8137-7894](https://orcid.org/0000-0001-8137-7894)

Qiang He: [0000-0002-3557-6865](https://orcid.org/0000-0002-3557-6865)

Author Contributions

Q.H. and M.C.Y. conceived the experiments; C.Y.G., C.Z., and Z.H.L. conducted the experiments; M.C.Y. worked out the

simulation; C.Y.G., M.C.Y., and Q.H. cowrote the manuscript. All authors commented on the manuscript. C.G. and C.Z. contributed equally.

Notes

The authors declare no competing financial interest.

ACKNOWLEDGMENTS

This work is financially supported by the National Natural Science Foundation of China (No. 21573053, 21674029) and National Postdoctoral Program for Innovative Talents (BX201700065).

REFERENCES

- (1) Qiu, T.; Lee, T.-C.; Mark, A. G.; Morozov, K. I.; Münster, R.; Mierka, O.; Turek, S.; Leshansky, A. M.; Fischer, P. Swimming by Reciprocal Motion at Low Reynolds Number. *Nat. Commun.* **2014**, *5*, 5119.
- (2) Larsen, S. H.; Reader, R. W.; Kort, E. N.; Tso, W.-W.; Adler, J. Change in Direction of Flagellar Rotation Is The Basis of The Chemotactic Response in *Escherichia Coli*. *Nature* **1974**, *249*, 74–77.
- (3) Wang, J. *Nanomachines: Fundamentals and Applications*; Wiley-VCH: Weinheim, Germany, 2013.
- (4) Dey, K. K.; Sen, A. Chemically Propelled Molecules and Machines. *J. Am. Chem. Soc.* **2017**, *139*, 7666–7676.
- (5) Sánchez, S.; Soler, L.; Katuri, J. Chemically Powered Micro- and Nanomotors. *Angew. Chem., Int. Ed.* **2015**, *54*, 1414–1444.
- (6) Wang, H.; Pumera, M. Fabrication of Micro/Nanoscale Motors. *Chem. Rev.* **2015**, *115*, 8704–8735.
- (7) Mei, Y. F.; Solovev, A. A.; Sánchez, S.; Schmidt, O. G. Rolled-Up Nanotech on Polymers: From Basic Perception to Self-Propelled Catalytic Microengines. *Chem. Soc. Rev.* **2011**, *40*, 2109–2119.
- (8) Sengupta, S.; Ibele, M. E.; Sen, A. Fantastic Voyage: Designing Self-Powered Nanorobots. *Angew. Chem., Int. Ed.* **2012**, *51*, 8434–8445.
- (9) Wang, W.; Chiang, T. Y.; Velegol, D.; Mallouk, T. E. Understanding The Efficiency of Autonomous Nano- and Microscale Motors. *J. Am. Chem. Soc.* **2013**, *135*, 10557–10565.
- (10) Ortiz-Rivera, I.; Mathesh, M.; Wilson, D. A. A Supramolecular Approach to Nanoscale Motion: Polymersome-Based Self-Propelled Nanomotors. *Acc. Chem. Res.* **2018**, *51*, 1891–1900.
- (11) Li, J. X.; de Avila, B. E. F.; Gao, W.; Zhang, L. F.; Wang, J. Micro/Nanorobots for Biomedicine: Delivery, Surgery, Sensing, and Detoxification. *Sci. Robot.* **2017**, *2*, No. eaam6431.
- (12) Gao, W. W.; de Avila, B. E. F.; Zhang, L. F.; Wang, J. Targeting and Isolation of Cancer Cells Using Micro/Nanomotors. *Adv. Drug Delivery Rev.* **2018**, *125*, 94–101.
- (13) Parmar, J.; Vilela, D.; Villa, K.; Wang, J.; Sánchez, S. Micro- and Nanomotors as Active Environmental Microcleaners and Sensors. *J. Am. Chem. Soc.* **2018**, *140*, 9317–9331.
- (14) Safdar, M.; Khan, S. U.; Janis, J. Progress Toward Catalytic Micro- and Nanomotors for Biomedical and Environmental Applications. *Adv. Mater.* **2018**, *30*, 1703660.
- (15) Kim, K.; Guo, J. H.; Liang, Z. X.; Fan, D. L. Artificial Micro/Nanomachines for Bioapplications: Biochemical Delivery and Diagnostic Sensing. *Adv. Funct. Mater.* **2018**, *28*, 1705867.
- (16) Zarei, M.; Zarei, M. Self-Propelled Micro/Nanomotors for Sensing and Environmental Remediation. *Small* **2018**, *14*, 1800912.
- (17) Palagi, S.; Fischer, P. Bioinspired Microrobots. *Nat. Rev. Mater.* **2018**, *3*, 113–124.
- (18) Peng, F.; Tu, Y. F.; Wilson, D. A. Micro/Nanomotors Towards In Vivo Application: Cell, Tissue and Biofluid. *Chem. Soc. Rev.* **2017**, *46*, 5289–5310.
- (19) Medina-Sanchez, M.; Xu, H. F.; Schmidt, O. G. Micro- and Nano-Motors: The New Generation of Drug Carriers. *Ther. Delivery* **2018**, *9*, 303–316.

- (20) Chalupniak, A.; Morales-Narvaez, E.; Merkoci, A. Micro and Nanomotors in Diagnostics. *Adv. Drug Delivery Rev.* **2015**, *95*, 104–116.
- (21) He, W. P.; Frueh, J.; Hu, N.; Liu, L. P.; Gai, M. Y.; He, Q. Guidable Thermophoretic Janus Micromotors Containing Gold Nanocolorifiers for Infrared Laser Assisted Tissue Welding. *Adv. Sci.* **2016**, *3*, 1600206.
- (22) Wang, W.; Castro, L. A.; Hoyos, M.; Mallouk, T. E. Autonomous Motion of Metallic Microrods Propelled by Ultrasound. *ACS Nano* **2012**, *6*, 6122–6132.
- (23) Dong, R. F.; Hu, Y.; Wu, Y. F.; Gao, W.; Ren, B. Y.; Wang, Q. L.; Cai, Y. P. Visible-Light-Driven BiOI-Based Janus Micromotor in Pure Water. *J. Am. Chem. Soc.* **2017**, *139*, 1722–1725.
- (24) Itel, F.; Schattling, P. S.; Zhang, Y.; Stadler, B. Enzymes as Key Features in Therapeutic Cell Mimicry. *Adv. Drug Delivery Rev.* **2017**, *118*, 94–108.
- (25) Patino, T.; Arque, X.; Mestre, R.; Palacios, L.; Sánchez, S. Fundamental Aspects of Enzyme-Powered Micro- and Nanoswimmers. *Acc. Chem. Res.* **2018**, *51*, 2662–2671.
- (26) Schattling, P. S.; Ramos-Docampo, M. A.; Salgueirino, V.; Stadler, B. Double-Fueled Janus Swimmers with Magnetotactic Behavior. *ACS Nano* **2017**, *11*, 3973–3983.
- (27) Ma, X.; Jannasch, A.; Albrecht, U. R.; Hahn, K.; Miguel-Lopez, A.; Schaffer, E.; Sánchez, S. Enzyme-Powered Hollow Mesoporous Janus Nanomotors. *Nano Lett.* **2015**, *15*, 7043–7050.
- (28) Arqué, X.; Romero-Rivera, A.; Feixas, F.; Patiño, T.; Osuna, S.; Sánchez, S. Intrinsic Enzymatic Properties Modulate The Self-propulsion of Micromotors. *Nat. Commun.* **2019**, *10*, 2826.
- (29) Dey, K. K.; Zhao, X.; Tansi, B. M.; Méndez-Ortiz, W. J.; Córdova-Figueroa, U. M.; Golestanian, R.; Sen, A. Micromotors Powered by Enzyme Catalysis. *Nano Lett.* **2015**, *15*, 8311–8315.
- (30) Abdelmohsen, L. K. E. A.; Nijemeisland, M.; Pawar, G. M.; Janssen, G.-J. A.; Nolte, R. J. M.; van Hest, J. C. M.; Wilson, D. A. Dynamic Loading and Unloading of Proteins in Polymeric Stomatocytes: Formation of An Enzyme-Loaded Supramolecular Nanomotor. *ACS Nano* **2016**, *10*, 2652–2660.
- (31) Joseph, A.; Contini, C.; Cecchin, D.; Nyberg, S.; Ruiz-Perez, L.; Gaitzsch, J.; Fullstone, G.; Tian, X.; Azizi, J.; Preston, J.; Volpe, G.; Battaglia, G. Chemotactic Synthetic Vesicles: Design and Applications in Blood-Brain Barrier Crossing. *Sci. Adv.* **2017**, *3*, No. e1700362.
- (32) Ma, X.; Hortelão, A. C.; Patiño, T.; Sánchez, S. Enzyme Catalysis to Power Micro/Nanomachines. *ACS Nano* **2016**, *10*, 9111–9122.
- (33) Chen, C. H.; Wang, H. Y.; Han, C. L.; Deng, J.; Wang, J.; Li, M. M.; Tang, M. H.; Jin, H. Y.; Wang, Y. Asymmetric Flasklike Hollow Carbonaceous Nanoparticles Fabricated by The Synergistic Interaction between Soft Template and Biomass. *J. Am. Chem. Soc.* **2017**, *139*, 2657–2663.
- (34) Parodi, A.; Quattrocchi, N.; van de Ven, A. L.; Chiappini, C.; Evangelopoulos, M.; Martinez, J. O.; Brown, B. S.; Khaled, S. Z.; Yazdi, I. K.; Vittoria Enzo, M.; Isenhardt, L.; Ferrari, M.; Tasciotti, E. Synthetic Nanoparticles Functionalized with Biomimetic Leukocyte Membranes Possess Cell-Like Functions. *Nat. Nanotechnol.* **2013**, *8*, 61–68.
- (35) Cao, X. D.; Yu, J. C.; Zhang, Z. Q.; Liu, S. Q. Bioactivity of Horseradish Peroxidase Entrapped in Silica Nanospheres. *Biosens. Bioelectron.* **2012**, *35*, 101–107.
- (36) Tu, Y. F.; Peng, F.; White, P. B.; Wilson, D. A. Redox-Sensitive Stomatocyte Nanomotors: Destruction and Drug Release in The Presence of Glutathione. *Angew. Chem., Int. Ed.* **2017**, *56*, 7620–7624.
- (37) Zhang, Y.; Zhang, L.; Yang, L.; Vong, C. I.; Chan, K. F.; Wu, W. K. K.; Kwong, T. N. Y.; Lo, N. W. S.; Ip, M.; Wong, S. H.; Sung, J. J. Y.; Chiu, P. W. Y.; Zhang, L. Real-Time Tracking of Fluorescent Magnetic Spore-Based Microrobots for Remote Detection of *C. diff* Toxins. *Sci. Adv.* **2019**, *5*, No. eaau9650.
- (38) Howse, J. R.; Jones, R. A. L.; Ryan, A. J.; Gough, T.; Vafabakhsh, R.; Golestanian, R. Self-Motile Colloidal Particles: From Directed Propulsion to Random Walk. *Phys. Rev. Lett.* **2007**, *99*, 048102.
- (39) Gao, L. Z.; Zhuang, J.; Nie, L.; Zhang, J. B.; Zhang, Y.; Gu, N.; Wang, T. H.; Feng, J.; Yang, D. L.; Perrett, S.; Yan, X. Intrinsic Peroxidase-Like Activity of Ferromagnetic Nanoparticles. *Nat. Nanotechnol.* **2007**, *2*, 577–583.
- (40) Anderson, J. L. Colloid Transport by Interfacial Forces. *Annu. Rev. Fluid Mech.* **1989**, *21*, 61–99.
- (41) Truesdell, R.; Mammoli, A.; Vorobieff, P.; van Swol, F.; Brinker, C. J. Drag Reduction on A Patterned Superhydrophobic Surface. *Phys. Rev. Lett.* **2006**, *97*, 044504.
- (42) Xuan, M.; Mestre, R.; Gao, C.; Zhou, C.; He, Q.; Sánchez, S. Noncontinuous Super-Diffusive Dynamics of A Light-Activated Nanobottle Motor. *Angew. Chem., Int. Ed.* **2018**, *57*, 6838–6842.
- (43) Malevanets, A.; Kapral, R. Mesoscopic Model for Solvent Dynamics. *J. Chem. Phys.* **1999**, *110*, 8605–8613.
- (44) Kapral, R. Multiparticle Collision Dynamics: Simulation of Complex Systems on Mesoscales. *Adv. Chem. Phys.* **2008**, *140*, 89–146.
- (45) Noguchi, H.; Kikuchi, N.; Gompper, G. Particle-Based Mesoscale Hydrodynamic Techniques. *Europhys. Lett.* **2007**, *78*, 10005.
- (46) Yang, M. C.; Wysocki, A.; Ripoll, M. Hydrodynamic Simulations of Self-Phoretic Microswimmers. *Soft Matter* **2014**, *10*, 6208–6218.
- (47) Ruckner, G.; Kapral, R. Chemically Powered Nanodimers. *Phys. Rev. Lett.* **2007**, *98*, 150603.